Applied Physics A (2023) 129:460
https://doi.org/10.1007/s00339-023-06738-3

Applied Physics A
Materials Science & Processing

Synthesis, characterization, and electromagnetic properties of polypyrrole–barium hexaferrite composites for EMI shielding applications

K. A. Darwish[1] · O. M. Hemeda[1] · M. I. Abdel Ati[1] · Anwer S. Abd El-Hameed[2] · Di Zhou[3] · Moustafa A. Darwish[1] · M. M. Salem[1]

Received: 28 March 2023 / Accepted: 20 May 2023 / Published online: 2 June 2023

Abstract
The purpose of this study was to evaluate the electromagnetic (EM) properties of hybrid materials made from polypyrrole (PPy) and barium hexaferrite (HF) for possible use in electromagnetic interference (EMI) shielding applications. X-ray diffraction and Fourier-transform infrared spectroscopy methods were used to confirm the presence of PPy and HF phases inside the hybrid structure. A scanning electron microscope analysis revealed that the HF particles were evenly dispersed throughout the PPy structure. The composites' dielectric and magnetic attributes were evaluated across a spectrum of frequencies, with the highest values observed in the PPy specimen. Adding HF to the PPy matrix altered the dielectric and magnetic properties of the composite, with the percentage of HF in the composite influencing its dominance over these properties. It was determined that a 25% HF content produced the most stable and efficient composite for absorbing EM waves in the X-band. This study demonstrates the potential of conductive polymer composites for EMI shielding applications, with advantages, such as improved EMI shielding, lightweight, flexibility, corrosion resistance, and tailored properties. The novelty lies in optimizing the composition of the PPy/HF composite and the characterization of its EM properties, providing insights into the design of more efficient EMI shielding materials.

Keywords Hexaferrite · Polypyrrole · Composites · Electromagnetic shielding

1 Introduction

Research into conductive polymer composites has received significant momentum as a dynamically developing topic. This is largely because of the composites' remarkable electrical and ferromagnetic characteristics. Batteries, supercapacitors, electrochemical displays, molecular electronics, electromagnetic shielding, and microwave absorption are just a few of the many possible uses for these substances. Notably, the use of conductive polymer composites in microwave absorption materials has attracted considerable interest, given the increasing prevalence of GHz-range microwave radiation in communication devices and associated concerns about electromagnetic interference (EMI) [1–4]. The need for efficient EMI shielding has surged in recent years, as the widespread adoption of communication devices operating in the GHz-range microwave radiation spectrum has led to higher data transfer speeds. Consequently, EMI has emerged as a pressing issue, driving demand for materials capable of providing effective shielding against it [2, 5–7].

One promising EMI shielding approach is combining conducting polymers and ferrite materials. Ferrites are magnetic materials with excellent magnetic properties, while conducting polymers offer strong electrical conductivity and high dielectric loss factors. Conductive polymer composites have several advantages in various applications, including lightweight, flexibility, corrosion resistance, and tunable electrical and magnetic properties. For example, in

✉ M. M. Salem
elshshtawy@science.tanta.edu.eg

[1] Physics Department, Faculty of Science, Tanta University, Tanta 31527, Egypt

[2] Electronics Research Institute, Giza 12622, Egypt

[3] Electronic Materials Research Laboratory, Key Laboratory of the Ministry of Education and International Center for Dielectric Research, School of Electronic Science and Engineering, Xi'an Jiaotong University, Xi'an 710049, China

EMI shielding applications, they offer comparable shielding effectiveness to traditional metal-based materials but with lower weight and greater flexibility, making them suitable for portable electronic devices. However, they may have lower thermal stability and mechanical strength than traditional materials, which could be a disadvantage in some applications [8, 9].

The composite material produced as a result of combining ferromagnetic nanoparticles with polymers is lightweight, flexible, and exhibits superior microwave properties in comparison with intrinsic ferrites and polymers. Polymer magnetic composites, which comprise ferromagnetic nanoparticles, have emerged as a particularly promising category of materials for EMI shielding. These materials exhibit strong EMI shielding performance and hold considerable promise for diverse applications, including molecular electronics and microwave absorption materials [5, 10–12].

Our study has investigated using relatively simple ($BaFe_{12}O_{19}$) HF/PPy (polypyrrole) nanocomposites for EMI shielding. The resulting HF/PPy nanocomposite was highly dispersed and compatible with the polymer matrix, making it highly effective for various applications. The synthesis of HF/PPy nanocomposites involves preparing HF nanoparticles using a simple auto-combustion procedure. The aqueous medium-based oxidative polymerization of pyrrole facilitates the incorporation of HF powder with PPy, forming a well-dispersed nanocomposite compatible with the polymer matrix [10, 13–16].

HF/PPy nanocomposites have been shown to exhibit excellent EM wave performance across a wide frequency range of 8–12 GHz (X-band), making them an effective solution for EMI shielding. Their unique properties arise from the combination of the magnetic and electrical components, resulting in a highly effective absorber of microwave radiation [10, 17, 18]. In comparison with other EMI shielding materials, such as metals or carbon-based materials, they offer a unique combination of properties but may require more optimization to achieve the desired performance at a competitive cost [19, 20].

Overall, the use of conducting polymer composites and ferrite materials in HF/PPy nanocomposites offers a highly innovative and effective approach to EMI shielding and other applications. This class of materials holds significant promise for advancing the field of electronics. Further research in this area will yield more breakthroughs and refine these materials. As the need for effective EMI shielding continues to grow, developing materials such as HF/PPy nanocomposites will be important in addressing this challenge. In addition, HF/PPy nanocomposites can be suitable for batteries and supercapacitors due to their high electrical conductivity, large surface area, and ability to store charge through both capacitive and faradaic mechanisms. These properties can lead to improved energy storage performance, higher power density, and faster charge–discharge rates compared to conventional materials. In addition, their lightweight and flexibility make them attractive for use in portable and wearable devices.

2 Experimental

2.1 Preparation of barium hexaferrite (HF)

This study synthesized $BaFe_{12}O_{19}$ (HF) nano hexaferrite using a simple auto-combustion technique. A stoichiometric blend of 1 mol of $Ba(NO_3)_2$ (barium nitrate), 12 mol of $Fe(NO_3)_3{\cdot}9H_2O$ (ferric nitrate), and 13 mol of $C_6H_8O_7$ (citric acid) was prepared. Subsequently, 250 ml of distilled water was added, and the mixture was agitated for 20 min using a hot plate magnetic stirrer. The pH was adjusted to 7 by incorporating an NH_4OH (ammonia solution). The mixture was then continuously stirred as the temperature was progressively raised to 110 °C and maintained until the solvent evaporated, leaving a residue. Finally, the resulting material was sintered at 1100 °C for a duration of 4 h [21].

2.2 Preparation of pure polypyrrole (PPy)

The chemical oxidative polymerization method was utilized to synthesize PPy using pyrrole monomer, HCl (hydrochloric acid), and $FeCl_3$ (anhydrous ferric chloride) as the oxidant. The procedure entailed combining the pyrrole monomer with 1 ml of HCl and stirring for 15 min. After that, $FeCl_3$ solution was added dropwise at a molar ratio (monomer:oxidant) of 1:2.33. The HCl functioned as a proton source, promoting the oxidation of pyrrole and enabling the formation of the PPy polymer while also affecting the electrical conductivity of the resulting polymer [22, 23]. Subsequent to adding the reaction solution, the mixture was placed in an ice bath, and the temperature was maintained between 1 and 7 °C [24]. The polymerization process began when the solution's color changed from clear to dark green. After 2 h of agitation at room temperature, the resultant powder was filtered, washed with distilled water to eliminate any remaining impurities, and then dried at 60 °C for 24 h.

Interestingly, HF nanoparticles are typically synthesized using methods, such as auto-combustion, sol–gel, or hydrothermal processes. PPy is usually synthesized via oxidative polymerization of pyrrole. Challenges in scaling up the production of these materials could include maintaining a consistent quality and size distribution of the nanoparticles, as well as controlling the polymerization process to achieve the desired properties in PPy. Further research and optimization of synthesis methods will be necessary to address these challenges.

2.3 Composites preparation

In accordance with Sect. 2.2, three composite samples containing (x) wt% PPy/($100-x$) wt% HF (where $x=25\%$, 50%, and 75%) were synthesized through in-situ oxidative chemical polymerization using optimized HF nanoparticles.

2.4 Characterizations

To analyze the composition of the prepared samples, X-ray diffraction (XRD) was carried out at room temperature ($20° \le 2\theta \le 80°$, Cu-K_α, $\lambda = 1.54$ Å) employing an Empyrean Panalytical diffractometer. The samples' composition was further assessed using Fourier-transform infrared spectroscopy (FTIR), which was conducted with a JASCO FT/IR4100 Series instrument measuring from 400 to 4000 cm^{-1}. The surface microstructure of all synthesized samples was examined using a scanning electron microscope (SEM) (Zeiss EVO 10, Oberkochen, Germany). At room temperature, a Lake Shore 7410 vibrating sample magnetometer (VSM) was used to detect the magnetic properties of the prepared samples using an applied magnetic field up to ± 2 T.

A Rohde & Schwarz ZVA67 vector network analyzer (VNA) with a waveguide WR-90 (sample dimensions $22.8 \times 10.1 \times 2$ mm^3) was used to examine electrical and magnetic parameters necessary for determining EM shielding properties was used to analyze the samples within the 8.2–12.4 GHz range. The VNA underwent full 2-port calibration (comprehensive calibration for all S-parameters S_{11}, S_{12}, S_{22}, and S_{21}). Using the observed S-parameters and the transmission/reflection line approach with the Nicolson–Ross–Weir algorithm, we determined the real and imaginary components of the permittivity and permeability. Using S-parameters from Eqs. 1, 2, 3, and 4, we were able to calculate the shielding efficiency due to reflection (SE_R), the shielding efficiency due to absorption (SE_A), and the total shielding efficiency (SE_T) [25–30]:

$$SE_R(dB) = -10\log\left(\frac{T}{1-R}\right) \quad (1)$$

$$SE_A(dB) = -10\log(1-R) \quad (2)$$

$$SE_T(dB) = -10\log\left(\frac{1}{T}\right) \quad (3)$$

$$T = |S_{12}|^2 = |S_{21}|^2, \quad R = |S_{11}|^2 = |S_{22}|^2. \quad (4)$$

The transmission and reflection coefficients are denoted by T and R, respectively. It is important to note that the samples being studied are homogeneous, which means that S_{11} is equal to S_{22} and S_{12} is equal to S_{21} [31].

3 Results and discussion

3.1 X-ray diffraction (XRD) discussion

The XRD patterns of PPy, HF, and PPy/HF composites were analyzed and presented in Fig. 1. The peaks observed in the XRD pattern of HF were also present in the prepared PPy/HF composites, indicating the presence of HF nanoparticles in the composite material. The main peak of HF was observed at 34°, corresponding to the (114) reflection [32–35]. This peak was also observed in the PPy/HF composites. On the other hand, the broad main peak of PPy was observed at 26° [34, 36]. Still, this peak was not observed well in the XRD for PPy/HF composites due to its low intensity and broadening, so the FTIR spectroscopy technique was used to clarify this issue. All the observed peaks in the XRD patterns of HF and PPy/HF composites were consistent with the JCPDS card no. 00-043-0002. This indicates that the crystal structure of all the samples was M-type hexagonal with space group P63/mmc. These results confirmed the presence of the M-type hexagonal crystal structure in all samples, consistent with previous studies on similar materials. The XRD patterns of the PPy/HF composites showed peaks at the same locations as those seen in HF, indicating that the crystal structure of HF was unaffected by the in-situ polymerization process of PPy. More ferrite nanoparticles were found to result in a greater intensity of all diffracted peaks in the PPy matrix. As the percentage of ferrite nanoparticles in the polymer composite rose, more crystalline structures emerged. All diffracted peaks were weaker in the PPy/HF composite than they were in pure HF, indicating that the

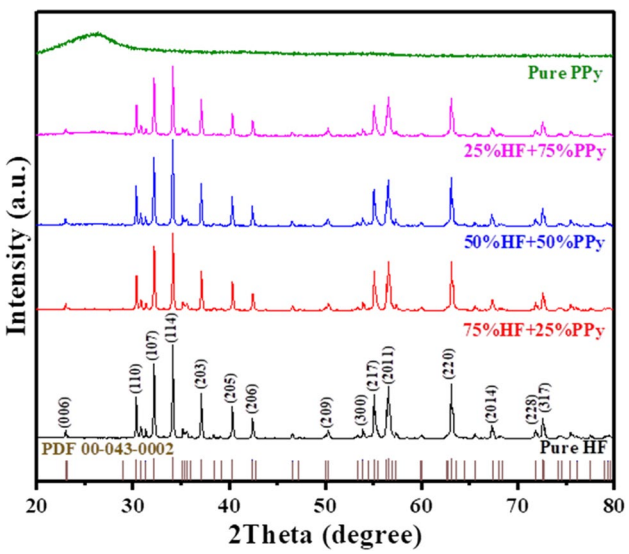

Fig. 1 XRD of all prepared samples

PPy contained the HF nanoparticles. The crystallite size of the PPy/HF nanocomposite particles was determined using Scherrer's formula, which establishes a relationship between the crystallite size and the line broadening measured by the peak's full width at half-maximum. This formula was applied to the XRD pattern's most prominent and intense peak, i.e., (114). The average crystallite size was in the range of 85 nm for the HF and PPy/HF nanocomposite.

3.2 Fourier-transform infrared (FTIR) spectroscopy discussion

Figure 2 presents the FTIR spectrum of all synthesized samples, revealing characteristic HF and PPy transmission bands, confirming the presence of both materials in the prepared composites. The FTIR spectrum of pure PPy exhibited characteristic peaks at 588 cm^{-1}, 1417 cm^{-1}, 1564 cm^{-1}, 2924 cm^{-1}, and 3446 cm^{-1}. The peak at 588 cm^{-1} is ascribed to the bending vibrations of the C–H bonds in the pyrrole rings of PPy [37]. The peak at 1417 cm^{-1} can be attributed to the bending vibrations of the C–H bonds in the polymer's pyrrole rings, while the peak at 1564 cm^{-1} corresponds to the stretching vibrations of the C=C bonds [38] in the pyrrole rings of PPy. The peak at 3446 cm^{-1} is associated with the stretching vibrations of N–H bonds [39], which are typically not observed in PPy.

The FTIR spectrum of the PPy/HF composite displayed two intense transmission bands at approximately 439 cm^{-1} and 596 cm^{-1}, identified as the metal–oxygen stretching vibrations of HF [40–43]. These bands indicate the presence of HF in the PPy/HF composite.

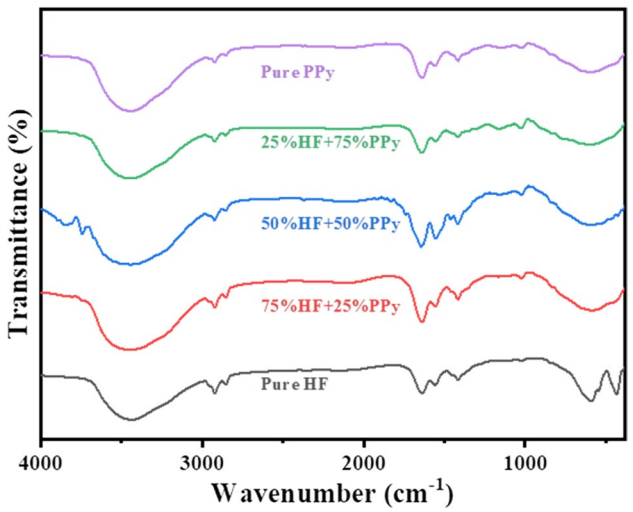

Fig. 2 FTIR of all prepared samples

3.3 SEM discussion

Figure 3 displays the morphology of PPy, HF, and PPy/HF composites with different weight ratios as observed through SEM. The SEM image of PPy shows that the PPy particles have a relatively uniform shape. Upon introducing HF nanoparticles into the PPy matrix, a good dispersion of HF nanoparticles was observed at 50 wt% mixing. However, at 75 wt% mixing, minor accumulation started to occur, and significant accumulation between HF nanoparticles and PPy was observed, leading to the formation of PPy/HF nanocomposite clusters. In the 75 wt% PPy/25 wt% HF composite sample, PPy effectively encapsulated the HF nanoparticles, and composite particles exhibited an asymmetrical shape with an irregular surface, forming composite nanoparticle clusters. The SEM images suggest that the PPy/HF composite's morphology depends on the weight ratio of the two components. The satisfactory dispersion of HF nanoparticles at less than or equal to 50 wt% of HF mixing implies that the composite may exhibit improved properties, such as enhanced conductivity, due to an extreme surface area [24, 44].

Moreover, the composite's permittivity, which is a material's capacity to store electrical energy in an electric field, may be higher by including HF nanoparticles [45, 46]. This increased permittivity can enhance the dielectric properties of the composite. However, the strong accumulation observed at 75 wt% of HF mixing may lead to decreased surface area and inferior properties. In this case, the shielding properties of the prepared samples may become more important. Overall, the SEM images provide important information on the morphology of the PPy/HF composite, which can be used to optimize the weight ratio of the two components to achieve the desired properties, such as enhanced conductivity or shielding properties.

3.4 VSM discussion

Figure 4 shows the measured VSM results. A material's coercivity (H_c) is the magnetic field required to demagnetize the material. In the case of the PPy/HF nanocomposite, the coercivity increases as the PPy content increases and gives maximum coercivity at 50 wt% of PPy and then decreases by increasing the PPy content, as shown in Table 1. At low PPy content, the nanoparticles are well-dispersed in the PPy matrix, leading to a strong interaction between the nanoparticles and the PPy matrix. This interaction results in a high H_c value due to the strong magnetic properties of the HF nanoparticles. However, as the PPy content increases, the nanoparticles become more dispersed in the polymer matrix, resulting in weaker interactions between the nanoparticles and the PPy matrix. This leads to a decrease in H_c value as the magnetic properties of the composite weaken.

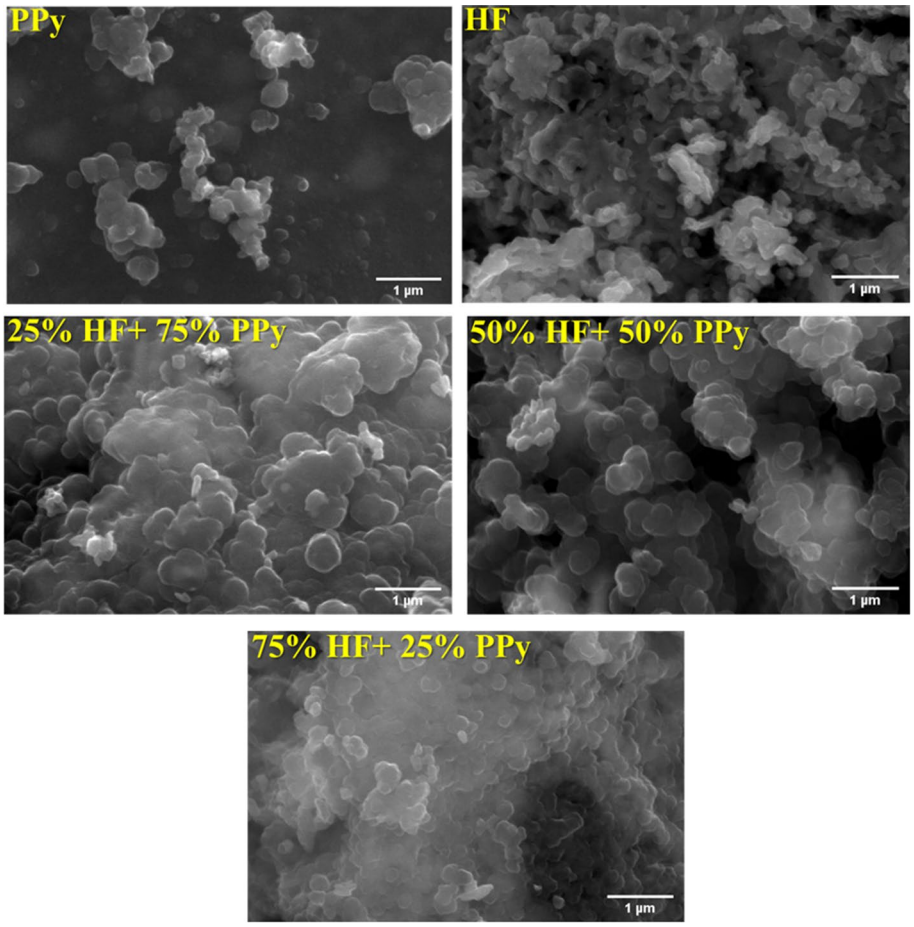

Fig. 3 SEM of all prepared samples

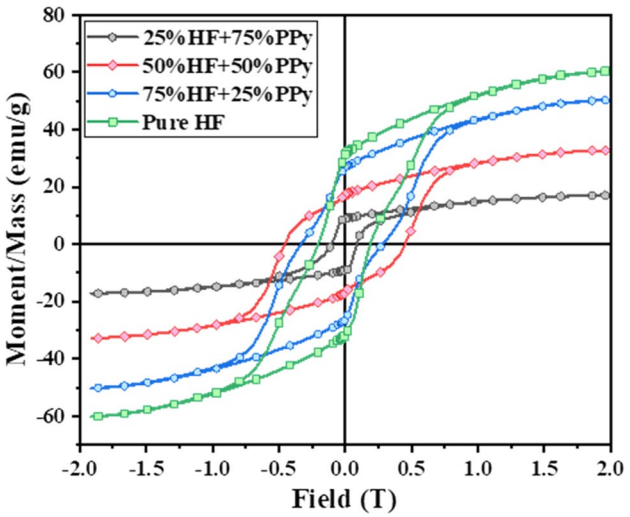

Fig. 4 VSM of the prepared HF and PPy/HF composites

Therefore, the decrease in H_c with increasing PPy content is due to the weaker interaction between the nanoparticles and the polymer matrix and the lower magnetic susceptibility of PPy compared to HF. The decrease in H_c of the PPy/HF nanocomposite with increasing PPy content can be attributed to several factors. First, the addition of PPy to the composite alters its microstructure. With a low PPy content, nanoparticles are effectively distributed within the PPy matrix, resulting in substantial interactions between the nanoparticles and the PPy matrix. This interaction leads to an elevated H_c value due to the powerful magnetic characteristics of the HF nanoparticles. However, as the proportion of PPy increases, the nanoparticles become more dispersed within the polymer matrix, leading to diminished interactions between the nanoparticles and the PPy matrix. Consequently, the H_c value decreases as the composite's magnetic properties weaken.

Table 1 Main magnetic properties of the prepared samples at room temperature using VSM

Sample	M_s (emu/g)	H_c (T)	M_r (emu/g)
HF	60.38	0.19	32.28
75% HF + 25% PPy	50.28	0.34	28.44
50% HF + 50% PPy	32.75	0.41	17.50
25% HF + 75% PPy	17.07	0.11	8.97

Moreover, the magnetic susceptibility of PPy is inferior to that of HF, implying that the inclusion of PPy in the composite diminishes the material's overall magnetic properties. As the PPy content within the composite rises, the PPy proportion increases, resulting in a decline in the composite's overall magnetic properties and a subsequent reduction in H_c.

Finally, the presence of PPy may disrupt the arrangement of magnetic domains within the composite, potentially contributing to the decreased H_c value. In magnetic materials, magnetic domains are regions, where magnetic moments align in a uniform direction. The organization of these domains is crucial for the material's overall magnetic properties. However, the presence of PPy could interfere with the alignment of these domains, causing a weaker magnetic response and a reduction in H_c.

In summary, the decrease in H_c with increasing PPy content in the PPy/HF nanocomposite can be attributed to a combination of factors, including the alteration of the microstructure, the lower magnetic susceptibility of PPy compared to HF, and the interference with the alignment of magnetic domains. As PPy is a conductive (non-magnetic) polymer, the remnant (M_r) and saturation magnetization (M_s) of the prepared composites depends on the HF content [47]. The saturation magnetization decreases by increasing PPy content, as shown in Table 1. Low saturation magnetization leads to high anisotropic energy (H_a) [48] according to the following equation [49]:

$$H_a = \text{constant} * \frac{K}{M_s}. \tag{5}$$

The anisotropic coefficient, denoted by K, is a factor that determines the degree of anisotropic energy present in the material. Higher anisotropic energy increases EM wave absorption within the high-frequency ranges [50].

3.5 Electro-magnetic properties

There could be several reasons why the results for the real and imaginary parts of permittivity and permeability are not arranged regularly by increasing the percentage of HF in the composites. Some possible factors that could affect the behavior of the composites include particle size and morphology: the size and shape of the HF particles could affect their distribution in the composite material and the interaction with the PPy matrix, leading to different permittivity and permeability values. Dispersion quality: the degree of dispersion of the HF particles in the PPy matrix could also play a role in determining the permittivity and permeability values. If the particles are not uniformly dispersed, this could lead to variations in the properties of the composite. Experimental conditions: the conditions under which the composites were prepared and measured could also affect the results. For example, temperature, pressure, and humidity differences during synthesis and testing could lead to variations in the properties of the composites. Interactions between materials: the interaction between the HF particles and the PPy matrix could also play a role in determining the permeability and permittivity values. The chemical and physical properties of the materials may interact in a complex manner, leading to non-linear behavior in the properties of the composites.

It is essential to acknowledge that the real part of permittivity and permeability relates to the material's energy storage capacity, while the imaginary part corresponds to the material's energy loss. In general, dielectric properties are improved through various polarization mechanisms, including space charge, interfacial, orientational, ion, and electron polarization. It is worth noting that ion and electron polarization primarily function at terahertz (THz) and petahertz (PHz) frequencies [51, 52]. The real part of permittivity can be enhanced through interfacial polarization caused by low-resistance grains separated by high-resistance grain boundaries. Polaron/bipolaron and interfacial polarization contribute to strong polarization within PPy, increasing the permittivity of samples containing HF [53, 54], as shown in Fig. 5. Observations suggest that the formation of agglomerates in samples containing over 25% HF can result in a non-uniform distribution of this phase in the composite samples. As a consequence, the permittivity of the samples may decrease, and the space charges and interfacial polarization can become weakened.

The real part of permeability, in general, decreases with increasing frequency. All the prepared samples are in the same range except the 25% barium hexaferrite sample, which has the lowest value, which could be explained by several factors: (1) magnetic properties of ferrite: HF has a high

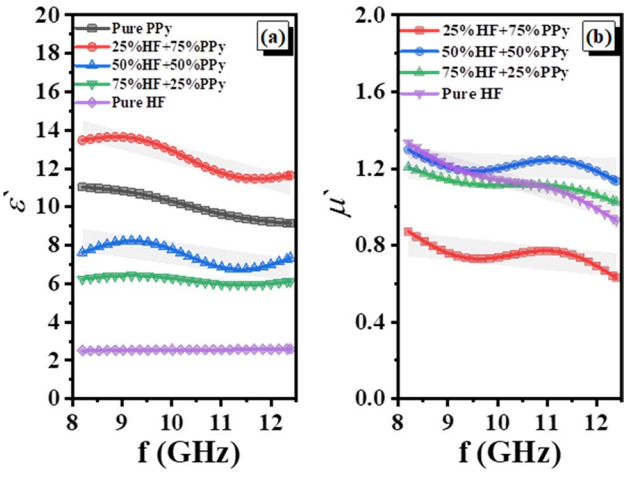

Fig. 5 Real part of permittivity (**a**) and permeability (**b**) of all prepared samples as a function of frequency

magnetic anisotropy, which means that its magnetic properties depend on the orientation of its magnetic moments concerning the crystal axes. At high frequencies, the orientation of the magnetic moments can become disordered, leading to a decrease in the real part of permeability. However, the effect of this disorder may be less pronounced in the 25% HF sample due to the lower amount of barium hexaferrite present. (2) Interfacial effects: the interface between the HF and PPy may also play a role in determining the permeability of the composite. At the optimal composition of 25% HF, the interface area between the two materials may be maximized, leading to the highest permittivity and lowest permeability values. To enhance the shielding efficiency due to absorption (SE_A), which follows the following relation, $SE_A \alpha \sigma \mu$ [49], it can find that improving the SE_A can be enhanced by increasing the conductivity (σ) and permeability (μ) of the studied samples, but there is a limit of increasing these parameters to obtain high SE_A. (3) Sample dimensions: the thickness of the sample can also influence the permeability values. If the sample is too thick, the magnetic moments may not have enough space to align with the magnetic field, leading to lower permeability values. Overall, the specific explanation for the trend in the real part of permeability values will depend on the specific properties of the materials used and the experimental conditions [17, 52, 54–60].

The decrease in imaginary part permittivity with increasing frequency is a common behavior in dielectric materials. It could be due to the relaxation of the dipoles in the material at higher frequencies. The fact that the imaginary part permittivity also decreased with the increasing percentage of HF may be due to the lower loss tangent of HF compared to PPy, leading to lower energy loss in the composite, as shown in Fig. 6.

The interface between the two materials may influence the imaginary part of permeability, leading to a different frequency dependence compared to the other samples. Magnetic properties of (HF): HF has a complex magnetic structure with multiple magnetic sublattices and domains. The magnetic behavior of the HF particles in the composite may influence the behavior of the imaginary part of permeability. At the optimal composition of 25% HF, the magnetic behavior of the HF particles may be different compared to the other samples, leading to a different frequency dependence [24, 54, 57, 60–65].

The dielectric and magnetic losses may not behave similarly depending on the frequency. This occurs, because the

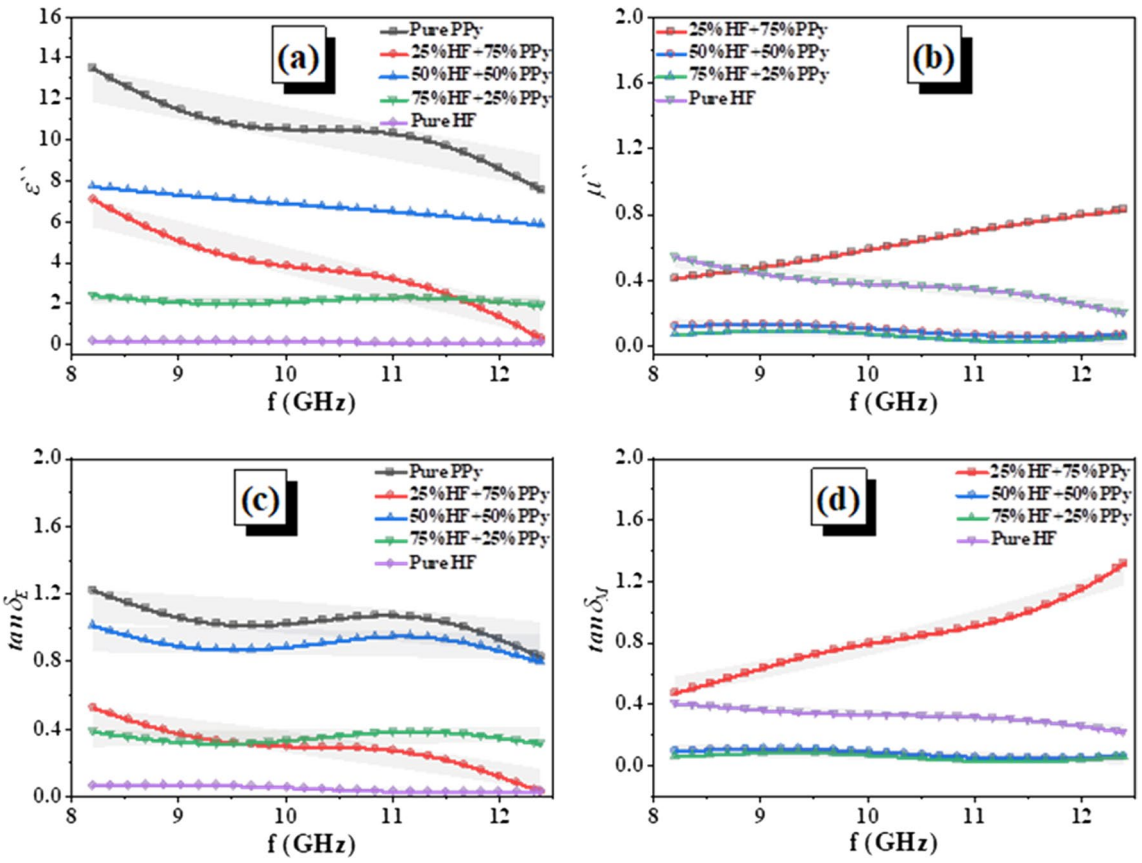

Fig. 6 Imaginary part of permittivity (**a**), the imaginary part of permeability (**b**), dielectric loss (**c**), and magnetic loss (**d**) of all prepared samples as a function of frequency

interaction between an electric field and a material results in the dissipation of electrical energy, which is measured as a dielectric loss. Nevertheless, the interaction between the material and the magnetic field results in a magnetic energy loss known as magnetic loss. Varying frequency dependencies result from these interactions being modified by various variables and processes. For instance, if an electric field polarises a magnetic and dielectric material, the dielectric loss may grow as the frequency rises.

In contrast, the magnetic loss may decrease with increasing frequency due to decreased magnetic domain rotation or relaxation time. However, other factors may influence the behavior of the dielectric and magnetic losses, such as the microstructure and composition of the material, the strength and orientation of the magnetic field, and the presence of interfaces or defects. When the distance between dielectric loss and magnetic loss values is minimal, EM wave absorption performance can reach maximum [52].

Figure 7 shows the relation between conductivity and frequency. The ac conductivity was calculated using the following equation [60]:

$$\sigma_{ac} = 2\pi f \varepsilon_o \varepsilon'' \quad (6)$$

where ε_o is the free space permittivity and equals 8.85×10^{-12} F/m.

PPy is a conductive polymer; adding it to HF can increase its conductivity. However, when the percentage of HF in the composite is too high, it may dominate the conductivity of the composite. The synthesis of PPy in the presence of HF can create a conductive phase network that enhances the material's electrical conductivity,

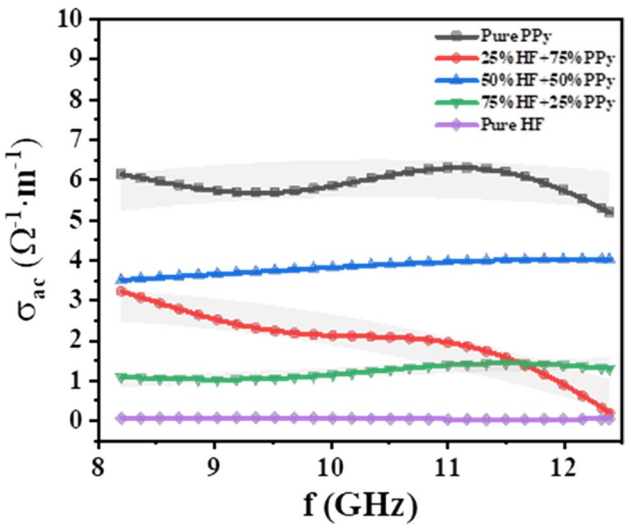

Fig. 7 Calculated ac conductivity of all prepared samples as a function of frequency

space charge, and interfacial polarization. As a result, the material's ability to store and dissipate electrical energy is improved [17, 52, 54–60].

The observed behavior where the highest values were obtained for the PPy sample and the values decreased with increasing amounts of barium hexaferrite in the composite can be explained by several factors, such as the effect of the HF particles on the electrical and magnetic properties of the composite material: the addition of HF to the PPy matrix can alter the dielectric and magnetic properties of the composite. As the percentage of HF in the composite increases, its influence on the properties of the composite becomes more dominant, leading to a decrease in the value of the measured property [17, 52, 54–60].

3.6 EM shielding properties

Figure 8 shows the shielding effectiveness of all prepared samples. It has been found that PPy has a high SE_A value due to its high dielectric loss [60, 66]. The SE_A value is the lowest in the HF sample. Adding PPy improves it by increasing the conductivity of HF and the number of free charge carriers, leading to greater polarizability and high ac conductivity, with a value of 12 dB for the 25% HF composite sample. In addition, by increasing the HF content, the SE_A began to decrease again, indicating the previous discussions that this kind of composite has an optimal percentage for adding the HF to obtain high SE_A. This percentage should not increase more than 25% HF. The SE_R for all prepared samples is less than 4.5, indicating that HF's SE_T enhanced due to absorption and reached 17 dB. It is worth mentioning that the prepared composites samples have high SE_A stability with frequency, especially for the 25% HF composite sample, which means that the ability to use this sample as an absorbing shield that covers the full frequency range in the X-band with SE_A more than 12 dB which can make more than 93% absorption efficiency [67] of the EM radiation in the X-band.

Composite materials consisting of conductive fillers have several benefits for EMI shielding applications. Many advantages may result from using these composites. Increased protection against EMI: the EMI shielding properties of HF may be significantly enhanced by adding conductive fillers. Lightweight: polymer composites are frequently significantly lighter than conventional EMI shielding materials based on metal, which might be useful when weight is a consideration. Flexibility: polymer composites can be designed to be more flexible and conformable than traditional EMI shielding materials, allowing for easier integration into complex shapes or curved surfaces. Corrosion resistance: unlike metal-based EMI shielding materials, polymer composites are not subject to corrosion, which can be an advantage in harsh environments. EM wave absorption: some conductive

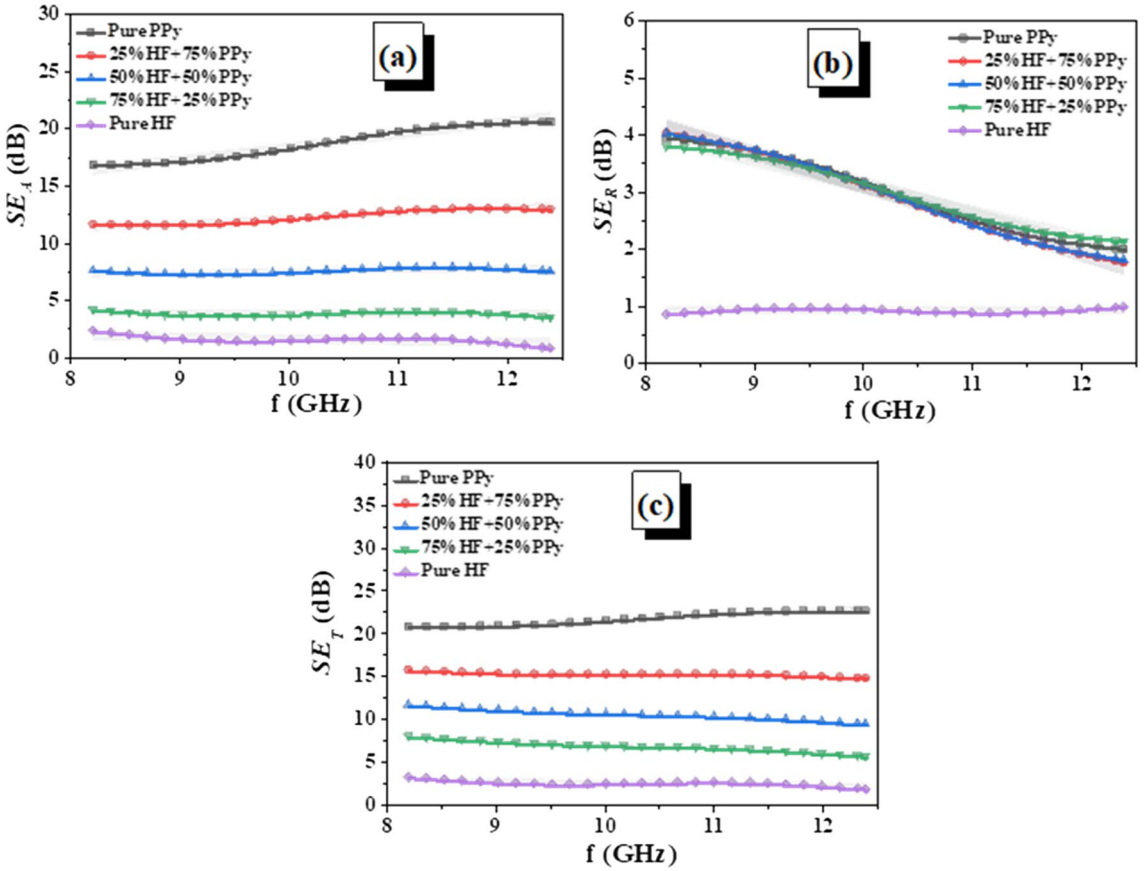

Fig. 8 Absorption (**a**), reflection (**b**), and total shielding (**c**) efficiency of all prepared samples

fillers can reflect and absorb EM waves, providing additional benefits for EMI shielding. Polymer composites may have their characteristics modified to suit a wide range of EMI shielding applications by altering the kind and concentration of conductive fillers [68].

4 Conclusions

XRD, FTIR, SEM, and VSM characterized the synthesized PPy/HF composites. XRD results indicated that the PPy/HF composites exhibited a polycrystalline structure, and the intensity of the peaks decreased as the percentage of HF in the composite increased. FTIR spectra revealed the presence of functional groups in the composites, and the peaks shifted to lower wavenumbers as the percentage of HF in the composite increased. SEM images showed that the composites had a rough surface and a porous structure. The morphology analysis showed that adding HF to the PPy matrix formed a network of conductive phases. Through investigation of the dielectric and magnetic properties of the composites, it was observed that adding HF to the PPy matrix increased electrical conductivity, space charge, and interfacial polarization. The composites showed an optimal percentage for adding HF, and this percentage should not exceed 25% HF to achieve the maximum EM wave absorption performance. The PPy/HF composites exhibited improved EMI shielding capabilities. They were lightweight, flexible, and corrosion-resistant, making them potential candidates for EMI shielding applications. Overall, the results indicate that the PPy/HF composites have tailored properties that can be adjusted to meet specific EMI shielding requirements.

Author contributions All authors contributed to the study conception and design. Material preparation, data collection and analysis were performed by KAD, OMH, MIAA, ASAE-H, DZ, MA and MMS. The first draft of the manuscript was written by KAD and all authors commented on previous versions of the manuscript. All authors read and approved the final manuscript.

Funding Open access funding provided by The Science, Technology & Innovation Funding Authority (STDF) in cooperation with The Egyptian Knowledge Bank (EKB).

Availability of data and materials The data sets generated during and/or analyzed during the current study are available from the corresponding author on reasonable request.

Declarations

Conflict of interest The authors declare that they have no known competing financial interests or personal relationships that could have appeared to influence the work reported in this paper.

References

1. H. Nguyen Cong, K. El Abbassi, J.L. Gautier, P. Chartier, Electrochim. Acta **50**, 1369 (2005)
2. A. Chen, H. Wang, B. Zhao, X. Li, Synth. Met. **139**, 411 (2003)
3. M. Kryszewski, J.K. Jeszka, Synth. Met. **94**, 99 (1998)
4. S. Tyagi, P. Verma, H.B. Baskey, R.C. Agarwala, V. Agarwala, T.C. Shami, Ceram. Int. **38**, 4561 (2012)
5. P. Bhattacharya, S. Dhibar, G. Hatui, A. Mandal, T. Das, C.K. Das, RSC Adv. **4**, 17039 (2014)
6. H. Nguyen-Cong, V. de la Garza Guadarrama, J.L. Gautier, P. Chartier, Electrochim. Acta **48**, 2389 (2003)
7. T.H. Ting, Y.N. Jau, R.P. Yu, Appl. Surf. Sci. **258**, 3184 (2012)
8. N. Maruthi, M. Faisal, N. Raghavendra, Synth. Met. **272**, 116664 (2021)
9. J.-M. Thomassin, C. Jérôme, T. Pardoen, C. Bailly, I. Huynen, C. Detrembleur, Mater. Sci. Eng. R Rep. **74**, 211 (2013)
10. D.A. Makeiff, T. Huber, Synth. Met. **156**, 497 (2006)
11. K.S. Jang, H. Lee, B. Moon, Synth. Met. **143**, 289 (2004)
12. N. Velhal, N. Patil, S. Jamdade, V. Puri, Appl. Surf. Sci. **307**, 129 (2014)
13. Y. Li, Y. Huang, S. Qi, L. Niu, Y. Zhang, Y. Wu, Appl. Surf. Sci. **258**, 3659 (2012)
14. B. Mušič, M. Drofenik, P. Venturini, A. Žnidaršič, Ceram. Int. **38**, 2693 (2012)
15. S.H. Hosseini, A. Asadnia, J. Nanomater. **2012**, 198973 (2012)
16. N.B. Velhal, N.D. Patil, V.R. Puri, J. Electron. Mater. **44**, 4669 (2015)
17. J. Luo, Y. Xu, H. Mao, J. Magn. Magn. Mater. **381**, 365 (2015)
18. N. Velhal, G. Kulkarni, N.D. Patil, V. Puri, Mater. Res. Express **5**, 106407 (2018)
19. Y. Ge, C. Li, G.I.N. Waterhouse, X. Jiang, Z. Zhang, L. Yu, Synth. Met. **274**, 116716 (2021)
20. S. Gupta, N.-H. Tai, Carbon N. Y. **152**, 159 (2019)
21. A.V. Trukhanov, K.A. Darwish, M.M. Salem, O.M. Hemeda, M.I. Abdel Ati, M.A. Darwish, E.Y. Kaniukov, S.V. Podgornaya, V.A. Turchenko, D.I. Tishkevich, T.I. Zubar, K.A. Astapovich, V.G. Kostishyn, S.V. Trukhanov, J. Alloys Compd. **866**, 158961 (2021)
22. P.H. Patil, V.V. Kulkarni, S.A. Jadhav, J. Compos. Sci. **6**, 363 (2022)
23. M. Beygisangchin, S. Abdul Rashid, S. Shafie, A.R. Sadrolhosseini, H.N. Lim, Polymers (Basel). **13**, 2003 (2021)
24. H.F. Shakir, M. Shahzad, H.R. Aziz, M.S. Rizwan, S. Shahid, S.H. Ali, T. Zhao, J. Alloys Compd. **902**, 163847 (2022)
25. J. Yang, X. Liao, J. Li, G. He, Y. Zhang, W. Tang, G. Wang, G. Li, Compos. Sci. Technol. **181**, 107670 (2019)
26. G. Wang, X. Liao, J. Yang, W. Tang, Y. Zhang, Q. Jiang, G. Li, Compos. Sci. Technol. **184**, 107847 (2019)
27. Z. Jia, K. Kou, S. Yin, A. Feng, C. Zhang, X. Liu, H. Cao, G. Wu, Compos. Part B Eng. **189**, 107895 (2020)
28. Y.-J. Tan, J. Li, J.-H. Cai, X.-H. Tang, J.-H. Liu, Z. Hu, M. Wang, Compos. Part B Eng. **177**, 107378 (2019)
29. Z. Jia, C. Wang, A. Feng, P. Shi, C. Zhang, X. Liu, K. Wang, G. Wu, Compos. Part B Eng. **183**, 107690 (2020)
30. A. Uddin, R. Khatoon, D. Estevez, M. Salem, A. Ali, S. Attique, J. Lu, F.X. Qin, Mater. Today Commun. **31**, 103858 (2022)
31. S. Sankaran, K. Deshmukh, M.B. Ahamed, S.K. Khadheer Pasha, Compos. Part A Appl. Sci. Manuf. **114**, 49 (2018)
32. K. Zubair, M.F. Shakir, A. Afzal, Z.A. Rehan, Y. Nawab, J. Supercond. Nov. Magn. **34**, 201 (2021)
33. R. Anum, M. Zahid, S. Siddique, H.M.F. Shakir, Z.A. Rehan, Synth. Met. **277**, 116773 (2021)
34. S. Siddique, M. Zahid, R. Anum, H.M.F. Shakir, Z.A. Rehan, Results Phys. **24**, 104183 (2021)
35. M. Zahid, S. Siddique, R. Anum, M.F. Shakir, Y. Nawab, Z.A. Rehan, J. Supercond. Nov. Magn. **34**, 1019 (2021)
36. M. Silakhori, H. Fauzi, M.R. Mahmoudian, H.S.C. Metselaar, T.M.I. Mahlia, H.M. Khanlou, Energy Build. **99**, 189 (2015)
37. Y. Wang, L. Li, J. Jiang, H. Liu, H. Qiu, F. Xu, React. Funct. Polym. **68**, 1587 (2008)
38. Q. Li, C. Zhang, Y. Wang, B. Li, Synth. Met. **159**, 2029 (2009)
39. P. Qiao, B. Zhao, Z. Nan, Mater. Sci. Eng. B **178**, 1476 (2013)
40. D. Sun, X. Jin, H. Liu, J. Zhu, Y. Zhu, Y. Zhu, Ferroelectrics **355**, 145 (2007)
41. S. Singhal, T. Namgyal, J. Singh, K. Chandra, S. Bansal, Ceram. Int. **37**, 1833 (2011)
42. S.T. Assar, H.F. Abosheiasha, D.-E.A. Mansour, M.A. Darwish, J. Alloys Compd. **821**, 153533 (2020)
43. M. Mostafa, O. Saleh, A.M. Henaish, S.A. Abd El-Kareem, R. Ghazy, O.M. Hemeda, A.M. Dorgham, H. Al-Ghamdi, A.H. Almuqrin, M.I. Sayyed, S.V. Trukhanov, E.L. Trukhanova, A.V. Trukhanov, D. Zhou, M.A. Darwish, Nanomaterials **12**, 1045 (2022)
44. D. Coetzee, M. Venkataraman, J. Militky, M. Petru, Polymers (Basel) **12**, 742 (2020)
45. J.-W. Zha, M.-S. Zheng, B.-H. Fan, Z.-M. Dang, Nano Energy **89**, 106438 (2021)
46. M.M. Forushani, G. Gordani, A. Ghasemi, M.R. Loghman Estarki, S. Torkian, H. Jamali, M. Tavoosi, E. Kiani, J. Mater. Res. Technol. **23**, 3424 (2023)
47. S. Mortazavinik, M. Yousefi, Russ. J. Appl. Chem. **90**, 298 (2017)
48. M.A. Darwish, V.A. Turchenko, A.T. Morchenko, V.G. Kostishyn, A.V. Timofeev, M.I. Sayyed, Z. Sun, S.V. Podgornaya, E.L. Trukhanova, E.Y. Kaniukov, S.V. Trukhanov, A.V. Trukhanov, J. Alloys Compd. **896**, 163117 (2022)
49. S. Acharya, P. Alegaonkar, S. Datar, Chem. Eng. J. **374**, 144 (2019)
50. S. Acharya, J. Ray, T.U. Patro, P. Alegaonkar, S. Datar, Nanotechnology **29**, 115605 (2018)
51. P. Liu, Z. Yao, J. Zhou, Ceram. Int. **42**, 9241 (2016)
52. A. Motamedi, R. Rahmanifard, M. Adibi, Synth. Met. **280**, 116873 (2021)
53. B. Belaabed, J.L. Wojkiewicz, S. Lamouri, N. El Kamchi, T. Lasri, J. Alloys Compd. **527**, 137 (2012)
54. F. Xu, L. Ma, M. Gan, J. Tang, Z. Li, J. Zheng, J. Zhang, S. Xie, H. Yin, X. Shen, J. Hu, F. Zhang, J. Alloys Compd. **593**, 24 (2014)

55. S.S. Seyyed Afghahi, M. Jafarian, M. Salehi, Y. Atassi, J. Magn. Magn. Mater. **421**, 340 (2017)
56. T. Guo, S. Chang, Y. Akinay, Synth. Met. **266**, 116387 (2020)
57. T. Chakraborty, S. Dutta, A.S. Mahapatra, K. Das, S. Das, A. Roy, M. Mukherjee, S. Das, S. Sutradhar, J. Magn. Magn. Mater. **570**, 170508 (2023)
58. M. Jafarian, S.S. Seyyed Afghahi, Y. Atassi, A. Loriamini, J. Magn. Magn. Mater. **493**, 165680 (2020)
59. T. Kaur, S. Kumar, S.B. Narang, A.K. Srivastava, J. Magn. Magn. Mater. **420**, 336 (2016)
60. N. Velhal, N.D. Patil, G. Kulkarni, S.K. Shinde, N.J. Valekar, H.C. Barshilia, V. Puri, J. Alloys Compd. **777**, 627 (2019)
61. S. Goel, A. Garg, H.B. Baskey, M.K. Pandey, S. Tyagi, J. Alloys Compd. **875**, 160028 (2021)
62. S.T. Assar, H.F. Abosheiasha, E.H. El-Ghazzawy, J. Alloys Compd. **802**, 553 (2019)
63. P.Y. Yu, Y.M. Kang, Curr. Appl. Phys. **31**, 99 (2021)
64. S.A. Mathews, D.R. Babu, Curr. Appl. Phys. **29**, 39 (2021)
65. Q. Li, Y. Chen, C. Yu, L. Young, J. Spector, V.G. Harris, Acta Mater. **231**, 117854 (2022)
66. A. Ohlan, K. Singh, A. Chandra, S.K. Dhawan, Appl. Phys. Lett. **93**, 53114 (2008)
67. D. Micheli, R. Pastore, A. Vricella, A. Delfini, M. Marchetti, F. Santoni, Chapter 9 - Electromagnetic characterization of materials by vector network analyzer experimental setup. In: S. Thomas, R. Thomas, A.K. Zachariah, R.K.B.T.-S.M. for N.C. Mishra (Eds.), Spectroscopic Methods for Nanomaterials Characterization. Micro and Nano Technologies (Elsevier, 2017), pp. 195–236. https://doi.org/10.1016/B978-0-323-46140-5.00009-1
68. M.A. Darwish, A.T. Morchenko, H.F. Abosheiasha, V.G. Kostishyn, V.A. Turchenko, M.A. Almessiere, Y. Slimani, A. Baykal, A.V. Trukhanov, J. Alloys Compd. **878**, 160397 (2021)